

Relativistic calculations of quasi-one-electron atoms and ions using Laguerre and Slater spinors

Jun Jiang*

*Key Laboratory of Atomic and Molecular Physics and Functional Materials of Gansu Province,
College of Physics and Electronic Engineering, Northwest Normal University, Lanzhou 730070, P. R. China and
School of Engineering, Charles Darwin University, Darwin NT 0909, Australia*

J. Mitroy†

School of Engineering, Charles Darwin University, Darwin NT 0909, Australia

Yongjun Cheng

*Academy of Fundamental and Interdisciplinary Science,
Harbin Institute of Technology, Harbin 150080, P. R. China and
School of Engineering, Charles Darwin University, Darwin NT 0909, Australia*

Michael W. J. Bromley‡

School of Mathematics and Physics, The University of Queensland, Brisbane, Queensland 4075, Australia

(Dated: July 9, 2018)

A relativistic description of the structure of heavy alkali atoms and alkali-like ions using S-spinors and L-spinors has been developed. The core wavefunction is defined by a Dirac-Fock calculation using an S-spinors basis. The S-spinor basis is then supplemented by a large set of L-spinors for the calculation of the valence wavefunction in a frozen-core model. The numerical stability of the L-spinor approach is demonstrated by computing the energies and decay rates of several low-lying hydrogen eigenstates, along with the polarizabilities of a $Z = 60$ hydrogenic ion. The approach is then applied to calculate the dynamic polarizabilities of the $5s$, $4d$ and $5p$ states of Sr^+ . The magic wavelengths at which the Stark shifts between different pairs of transitions are zero are computed. Determination of the magic wavelengths for the $5s \rightarrow 4d_{\frac{3}{2}}$ and $5s \rightarrow 4d_{\frac{5}{2}}$ transitions near 417 nm (near the wavelength for the $5s \rightarrow 5p_j$ transitions) would allow a determination of the oscillator strength ratio for the $5s \rightarrow 5p_{\frac{1}{2}}$ and $5s \rightarrow 5p_{\frac{3}{2}}$ transitions.

PACS numbers: 31.15.ac, 31.15.ap, 34.20.Cf

I. INTRODUCTION

This paper describes the development and application of a relativistic model for atomic structure. The basic strategy of the model is to partition the atom into valence and core electrons. The core electrons will be represented by orbitals obtained from Dirac-Fock calculations. The

wave function for the valence electrons will be computed by expanding the wave function as a linear combination of Laguerre function spinors (L-spinors) and Slater function spinors (S-spinors) [1–3]. The direct and exchange interactions between the core and valence electrons can be computed without approximation. Core-valence correlations can be represented by simply introducing semi-empirical core polarization potentials which are tuned to ensure that the energies for the valence electrons agree with experiment [4–6].

The motivation for this methodology is based on the

*Electronic address: phyjiang@yeah.net

†Deceased.

‡URL: <https://www.smp.uq.edu.au/people/brom/>

success of similar methodologies in computing atomic properties of light atoms, namely non-relativistic configuration interaction with a semi-empirical core potential method (CICP) [4–7]. As a recent example, the dipole polarizability of the Si^{2+} ion computed with a similar methodology is $11.688 a_0^3$ [8]. An analysis of a resonant excitation stark ionization spectroscopy (RESIS) [9] experiment give $11.669(9) a_0^3$ [8, 10] while a very sophisticated relativistic configuration interaction with many body perturbation theory calculation (MBPT) gave $11.670(13) a_0^3$ [11]. Numerous other examples of very good agreement of the semi-empirical method with the most advanced *ab-initio* theoretical models for oscillator strengths and polarizabilities can be found in Ref. [12–14].

There are a number of reasons for the success of the relativistic semi-empirical approach. Firstly, this approach is based on the *ab-initio* Dirac-Fock (DF) calculation to define the core. Secondly, tuning energies to experimental values leads to wave functions that have the correct asymptotic decay at long distances from the nucleus. The multipole matrix elements needed for oscillator strength and polarizability calculations tend to be dominated by the large- r form of the wave function. Finally, partitioning the wave function into frozen-core electrons and an active valence electron reduces the equation for the wave function and energies into one equation that admits a close to exact numerical solution, here using a large (orthogonal) Laguerre basis.

It should be noted that the DF+core-polarization method adopted here has been extensively used by Migdalek and co-workers to calculate the oscillator strengths of many atoms [15–18]. They solved the radial equations numerically [19], and they typically restricted their transitions to between those of the low-lying states. Here, we employ basis sets which enables the calculation of transition matrix elements between both the bound states and the continuum (pseudostates). This enables us here to compute atomic polarizabilities [20], where the continuum makes a significant contribution [6].

The present work gives a brief description of the strategy adopted to convert an existing non-relativistic

Hartree-Fock (HF) program [21] into a relativistic DF program. Next, the technical details for performing calculations for one valence electron atoms and ions are discussed. These methods are then applied to the solution of hydrogen and hydrogenic atoms as a test for evaluation.

The main results presented are the oscillator strengths, and static and dynamic polarizabilities for the low-lying states of Sr^+ ions. In addition some of the magic wavelengths for $5s-5p_J$ and $5s-4d_J$ transitions are presented, at which the ac-Stark shift of the transition energy is zero. The static polarizabilities of Sr^+ can be used to estimate frequency shifts of $5s-4d_J$ clock transitions due to background fields such as blackbody radiation shifts [22]. The magic wavelengths can be used, for example, for high-precision trapping measurements [23, 24]

II. FORMULATION AND VALIDATIONS

The single-electron Dirac equation can be written as,

$$H\Psi(\mathbf{r}) = E\Psi(\mathbf{r}), \quad (1)$$

where the Hamiltonian

$$H = c\boldsymbol{\alpha} \cdot \mathbf{p} + \beta c^2 - \frac{Z}{r} + V_{core}, \quad (2)$$

\mathbf{p} is the momentum operator, $\boldsymbol{\alpha}$ and β are 4×4 matrices of the Dirac operators [25]. The V_{core} represents the valence electron-core electrons interaction, and is described shortly.

We have two separate codes that we present the first results from here. The first is the DF calculation, which generates the closed-shell orbitals using purely Slater-type orbitals. The second code solves for a single valence electron orbiting the closed-shell using a mixture of the Slater-type orbitals produced by the first code with additional Laguerre-type orbitals to describe the valence electronic structure and continuum physics.

A. Calculations of core orbitals

The starting point of a calculation involving closed shells is the DF calculation for the core state of the atoms.

The DF equations are closely related to the HF equations. The atomic Schrödinger Hamiltonian is replaced by the Dirac-Coulomb Hamiltonian and the single particle orbitals are now 4-component spinors with a large and a small component.

The strategy used to generate a DF wave function is to adapt an existing HF program [21] which expands the orbitals as a linear combination of Slater (or Gaussian) type orbitals. The first stage of the modification is to generate the angular representation of the orbitals from $\ell \rightarrow \ell, j$ representation.

The next stage is to write each orbital in terms of S-spinors. Each orbital wavefunction can be written as

$$\psi_{n\kappa m}(\mathbf{r}) = \frac{1}{r} \begin{pmatrix} P_{n\kappa}(r)\Omega_{\kappa m}(\hat{\mathbf{r}}) \\ iQ_{n\kappa}(r)\Omega_{-\kappa m}(\hat{\mathbf{r}}) \end{pmatrix}, \quad (3)$$

where κ is the relativistic angular quantum number which is connected to the total angular momentum quantum number j and the orbital angular momentum quantum number ℓ ,

$$\kappa = \ell(\ell + 1) - j(j + 1) - \frac{1}{4}. \quad (4)$$

$P_{n\kappa}(r)$ and $Q_{n\kappa}(r)$ represent the large and small components of radial wavefunction, and $\Omega_{\kappa m}(\hat{\mathbf{r}})$ and $\Omega_{-\kappa m}(\hat{\mathbf{r}})$ are the angular components.

The radial wavefunctions $P_{n\kappa}(r)$ and $Q_{n\kappa}(r)$ are expanded as N -terms in an S-spinor basis

$$P_{n\kappa}(r) = \sum_{i=1}^N p_i \phi_{i,\kappa}^P(r), \quad Q_{n\kappa}(r) = \sum_{i=1}^N q_i \phi_{i,\kappa}^Q(r), \quad (5)$$

where the superscript P and Q identify the ‘‘large’’ and ‘‘small’’ components of the Dirac spinor in a conventional way.

Although it is common to formally sub-divide the basis functions into small and large type functions and explicitly recognize this when casting the DF equations into operational form [3], that approach is not adopted in the present paper. Instead, each orbital has a label identifying it as being of a large or small component in the present code. These labels are taken into account when computing the matrix elements of the DF Hamiltonian. This approach is adopted since minimal modifications are

needed for those parts of the program that construct and diagonalize the Hamiltonian. In effect, information about the spinor construction is confined to those parts of the program that evaluate the matrix elements of the basis functions.

S-spinors are generalizations of Slater type orbitals (STO) adapted to relativistic systems. The first modification is the inclusion of a radial r^γ pre-factor with

$$\gamma(\kappa) = \sqrt{\kappa^2 - Z^2/c^2} \quad (6)$$

to ensure these functions have the correct asymptotic form at origin. Here, Z is the atomic number and we adopt $c = 137.0359991$ as the speed of light (in atomic units).

The second modification includes choosing the large and small component basis functions to approximately satisfy the kinetic balance condition [2]. The unnormalized radial components are written as,

$$\phi_{i,\kappa}^{P,Q}(r) = r^\gamma e^{-\lambda_i r} \quad (7)$$

for orbitals with $\kappa < 0$, and

$$\phi_{i,\kappa}^{P,Q}(r) = A_{P,Q} r^\gamma e^{-\lambda_i r} + \lambda r^{\gamma+1} e^{-\lambda_i r} \quad (8)$$

for orbitals with $\kappa > 0$, where

$$A_P = \frac{(\kappa + 1 - \sqrt{\kappa^2 + 2\gamma + 1})(2\gamma + 1)}{2(\sqrt{\kappa^2 + 2\gamma + 1} - \kappa)} \quad (9)$$

for the large components and

$$A_Q = \frac{(\kappa - 1 - \sqrt{\kappa^2 + 2\gamma + 1})(2\gamma + 1)}{2(\sqrt{\kappa^2 + 2\gamma + 1} - \kappa)} \quad (10)$$

for the small components.

1. Numerical test: energy of closed-shell atoms

A DF basis set is formed as a collection of S-spinors with positive real exponents $\{\lambda_i\}$ and coefficients $\{p_i\}$ and $\{q_i\} \forall i = 1, 2, \dots, N_S$. that undergo variational optimization. The S-spinor for the orbitals with $\kappa < 0$ has a very simple form. The radial prefactor did not allow for additional powers of r as prefactors. This is distinct from

TABLE I: Comparison of numerical DF energies (in a.u.) of several closed-shell atoms and ions as computed with various S-spinor basis sets using the present S-spinor program and the GRASP92 program [27]. The notation $a[b]$ indicates $a \times 10^b$. The underlines denote the digits which are different from the two programs.

Atom/Ion	Basis Set	S-spinor	GRASP92
Li ⁺	7s	-7.237205 <u>25</u>	-7.23720552
Na ⁺	7s,4p	-1.618958 <u>77</u> [2]	-1.61895968[2]
K ⁺	8s,7p	-6.01378 <u>956</u> [2]	-6.01379058[2]
Rb ⁺	11s,8p,5d	-2.979693 <u>23</u> [3]	-2.97969324[3]
Cs ⁺	14s,12p,10d	-7.78694 <u>367</u> [3]	-7.78694284[3]
Ne	8s,5p	-1.28691 <u>836</u> [2]	-1.28691970[2]
Ar	11s,9p	-5.286844 <u>41</u> [2]	-5.28684451[2]
Kr	10s,9p,5d	-2.78888 <u>845</u> [3]	-2.78888486[3]
Xe	14s,12p,9d	-7.447162 <u>55</u> [3]	-7.44716272[3]
Be ²⁺	5s	-1.361399 <u>56</u> [1]	-1.36140014[1]
Mg ²⁺	9s,6p	-1.991501 <u>19</u> [2]	-1.99150137[2]
Ca ²⁺	10s,9p	-6.791050 <u>26</u> [2]	-6.79105063[2]
Sr ²⁺	12s,10p,5d	-3.177554 <u>10</u> [3]	-3.17755362[3]
Ba ²⁺	15s,14p,10d	-8.13548 <u>402</u> [3]	-8.13548296[3]

the related STO basis sets used for non-relativistic calculations which usually have radial prefactors with a variety of powers of r [26]. In our calculations, the S-spinor basis sets used are based on non-relativistic basis sets. An STO basis with all functions restricted to $n = \ell + 1$ was optimized for the non-relativistic calculation. Once the optimization was complete, this was modified by the replacement $n \rightarrow \sqrt{\kappa^2 - Z^2/c^2}$ for S-spinors. This is based on the form of the exact wave functions for $\kappa < 0$. No further minor optimizations is undertaken as the relativistic scf calculations are time consuming to do.

Table I gives DF energies computed using S-spinor basis and numerical DF energies computed using GRASP92 [27]. It can be seen that the two sets of energies are in agreement with each other to at least six significant digits. Note that GRASP92 uses a finite difference method, so such differences are expected. See Supplemental Table I, Table II, and Table III for lists of the basis exponents.

B. Calculation of valence orbitals

The orbitals for the valence electrons are written as linear combinations of S-spinors and L-spinors. L-spinors are generalizations of Laguerre type orbitals [28] adapted to relativistic systems, and they are derived from the relativistic analogues of Coulomb Sturmians [2]. The (un-normalized) L-spinors are written as

$$\phi_{i,\kappa}^P(r) = r^\gamma e^{-\lambda_i r} \left\{ (\delta_{n_i,0} - 1)L_{n_i-1}^{2\gamma}(2\lambda_i r) + BL_{n_i}^{2\gamma}(2\lambda_i r) \right\} \quad (11)$$

and

$$\phi_{i,\kappa}^Q(r) = r^\gamma e^{-\lambda_i r} \left\{ (\delta_{n_i,0} - 1)L_{n_i-1}^{2\gamma}(2\lambda_i r) - BL_{n_i}^{2\gamma}(2\lambda_i r) \right\}, \quad (12)$$

where the balanced coefficient

$$B = \frac{\sqrt{n_i^2 + 2n_i\gamma + \kappa^2} - \kappa}{n_i + 2\gamma}, \quad (13)$$

with n_i being a non-negative integer ($n_i \geq 0$ for $\kappa < 0$ and $n_i \geq 1$ for $\kappa > 0$), The L_n^α are Laguerre polynomials [29] which are computed using the recursion relation

$$L_{n+1}^\alpha(x) = \frac{(2n + \alpha + 1 - x)}{(n + 1)}L_n^\alpha(x) - \frac{(n + \alpha)}{(n + 1)}L_{n-1}^\alpha(x), \quad (14)$$

with $L_0^\alpha(x) = 1$ and $L_1^\alpha(x) = 1 + \alpha - x$. In our single-valence electron calculations, we always choose $2N$ L-spinor orbitals which include N large component orbitals and N small component orbitals.

The radial Dirac equation, Eqn. 1, can be solved as a (real, symmetric) matrix eigenproblem, with the resulting set of N eigenfunctions

$$\Psi_I(\mathbf{r}) = \sum_{n_I=1}^N c_{n_I} \psi_{n_I \kappa_I m_I}(\mathbf{r}), \quad (15)$$

where $I \in 1, \dots, N$. In order to compare with non-relativistic calculations, we replace the energy E by $\varepsilon = E - mc^2$, where m is the mass of the electron ($m = 1$ in atomic units).

1. Numerical test: energy of hydrogen atom

Our code was first tested by diagonalizing the ground state of hydrogen (ie. $Z = 1$, $V_{core} = 0$) with $N =$

TABLE II: Theoretical (RCI) energies (ε in Hartree) and separated E1 ($\Gamma^{(1)}$) and E2 ($\Gamma^{(2)}$) decay rates (in 1/nanoseconds) for several eigenstates of hydrogen. The underlines denote the digits which are different from the NIST tabulation [30]. The notation $a[b]$ indicates $a \times 10^b$.

I	j_I	ε_I	$\Gamma_I^{(1)}$	$\Gamma_I^{(2)}$
1s	$\frac{1}{2}$	-0.500 <u>0066566</u>	--	--
2s	$\frac{1}{2}$	-0.1250 <u>020802</u>	--	--
2p	$\frac{1}{2}$	-0.1250 <u>020802</u>	6.268 <u>31</u> [8]	--
	$\frac{3}{2}$	-0.1250 <u>04160</u>	6.268 <u>38</u> [8]	1.310[-22]
3s	$\frac{1}{2}$	-0.0555 <u>5629518</u>	6.31 <u>771</u> [6]	--
3p	$\frac{1}{2}$	-0.0555 <u>5629516</u>	1.898 <u>01</u> [8]	23.9212
	$\frac{3}{2}$	-0.0555 <u>580208</u>	1.898 <u>07</u> [8]	23.9214
3d	$\frac{3}{2}$	-0.0555 <u>580210</u>	6.468 <u>74</u> [7]	645.117
	$\frac{5}{2}$	-0.0555 <u>563772</u>	6.468 <u>64</u> [7]	645.125
4s	$\frac{1}{2}$	-0.031250 <u>33803</u>	4.416 <u>42</u> [6]	1.02876
4p	$\frac{1}{2}$	-0.031250 <u>33803</u>	8.131 <u>00</u> [7]	12.8530
	$\frac{3}{2}$	-0.031250 <u>13001</u>	8.131 <u>29</u> [7]	12.8534
4d	$\frac{3}{2}$	-0.031250 <u>13003</u>	2.767 <u>84</u> [7]	337.072
	$\frac{5}{2}$	-0.031250 <u>06066</u>	2.767 <u>79</u> [7]	337.078
4f	$\frac{7}{2}$	-0.031250 <u>06067</u>	1.379 <u>55</u> [7]	67.6017
	$\frac{5}{2}$	-0.031250 <u>02601</u>	1.379 <u>54</u> [7]	67.6014

50 L-spinors. A value of $\lambda = 2.0$ was chosen for the s orbitals and $\lambda = 1.0$ for other orbitals ($\lambda = 1.0$ would correspond to the exact hydrogen ground state). The results for several eigenstates of hydrogen are shown in Table II and compare well with the NIST (experimental) values [30], given that we are using the infinite proton mass approximation. These calculations were performed in quadruple precision arithmetic (also shown are their decay rates: these are discussed in the next section).

However, we can also compare the basis set convergence of the eigenenergy to the exact solution of the Dirac equation. For the states with $\kappa > 0$ ($2s_{\frac{1}{2}}, 2p_{\frac{3}{2}}, 3d_{\frac{5}{2}}$) the convergence patterns are all monotonic as shown in Fig. 1. Convergence is rapid and an accuracy of about 10^{-30} , is the achievable limit with quadruple precision arithmetic.

The convergence of the eigenenergy for the $2p_{\frac{1}{2}}$ and $3d_{\frac{3}{2}}$ states with increasing dimension of the L-spinor basis stalled at some point, as also seen in Fig. 1. The $2p_{\frac{1}{2}}$

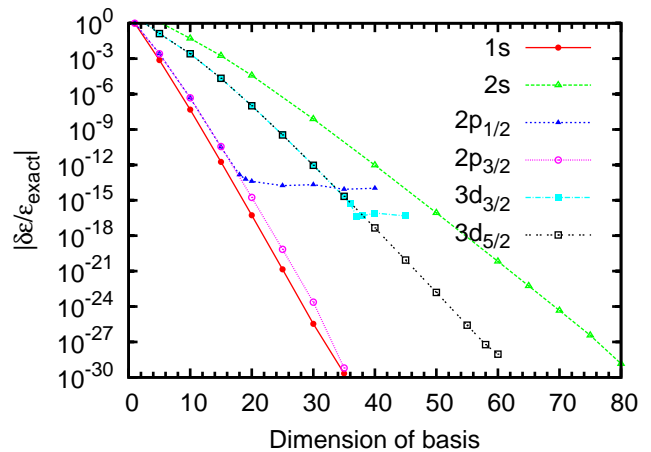


FIG. 1: (color online). The convergence of the energy of the low-lying hydrogen eigenstates relative to the exact energy $\delta\varepsilon/\varepsilon_{\text{exact}} = (\varepsilon - \varepsilon_{\text{exact}})/\varepsilon_{\text{exact}}$ as the dimension of the L-spinor basis is increased. The exponent in the L-spinor basis was set to $\lambda = 2.0$.

energy using the L-spinor representation actually goes below that of the exact energy at $N = 20$ by 5×10^{-15} Hartree. This is suspicious of a double precision limitation inside the code for $\kappa < 0$ states. However, despite experimentation with both EISPACK and LAPACK eigen-solvers we were unable to push below that of a purely double precision calculation. Thus, the remainder of the Sr^+ calculations shown in this paper are all computed in double precision, where the uncertainties relating to the core potential lie far above the limits established here.

C. Calculation of transition matrix elements

The 2^k -pole oscillator strength, $f_{IJ}^{(k)}$, from initial state Ψ_I to another eigenstate Ψ_J is defined as

$$f_{IJ}^{(k)} = \frac{2\varepsilon_{IJ} |\langle \Psi_I \| r^k \mathbf{C}^{(k)}(\hat{\mathbf{r}}) \| \Psi_J \rangle|^2}{(2k+1)(2j_I+1)}, \quad (16)$$

with $\varepsilon_{IJ} = E_J - E_I$ being the excitation energy, j_I is the total angular momentum for the initial state, and $\mathbf{C}^{(k)}(\hat{\mathbf{r}})$ is the k -th order spherical tensor. The line strength, $|\langle \Psi_I \| r^k \mathbf{C}^{(k)}(\hat{\mathbf{r}}) \| \Psi_J \rangle|^2$, is calculated via the reduced matrix elements between the orbitals

$$\langle \Psi_I \| r^k \mathbf{C}^{(k)}(\hat{\mathbf{r}}) \| \Psi_J \rangle = \sum_{n_I, n_J} c_{n_I} c_{n_J} \langle \psi_{n_I} \| r^k \mathbf{C}^{(k)}(\hat{\mathbf{r}}) \| \psi_{n_J} \rangle, \quad (17)$$

whose (orbital) matrix elements split into a radial part

$$\begin{aligned} & \langle \psi_{n_I}(r) | r^k | \psi_{n_J}(r) \rangle \\ &= \int_0^\infty \frac{r^k}{r^2} [P_{n_I}(r)P_{n_J}(r) + Q_{n_I}(r)Q_{n_J}(r)] r^2 dr, \end{aligned} \quad (18)$$

multiplied by an angular part [3]

$$\begin{aligned} \langle \Omega_{\kappa_I}(\hat{\mathbf{r}}) | \mathbf{C}^{(k)} | \Omega_{\kappa_J}(\hat{\mathbf{r}}) \rangle &= (-1)^{j_I + \frac{1}{2}} \sqrt{(2j_I + 1)(2j_J + 1)} \\ &\times \begin{pmatrix} j_I & j_J & k \\ -\frac{1}{2} & \frac{1}{2} & 0 \end{pmatrix}. \end{aligned} \quad (19)$$

1. Numerical test: lifetimes of hydrogen atom

The lifetime of a given state Ψ_I is computed as

$$\tau_I = (\Gamma_I)^{-1} = \left(\sum_{k=1}^2 \Gamma^{(k)} \right)^{-1}, \quad (20)$$

ie. here the decay rate Γ_I consists only of E1 ($k = 1$ dipole) and E2 ($k = 2$ quadrupole) pathways. The transition probabilities (in s^{-1}) can be written as [31, 32]

$$A^{(k)} = A_0 \frac{\varepsilon_{IJ}^{2k+1}}{(2j_I + 1)c^{2k+1}} |\langle \Psi_I | r^k \mathbf{C}^{(k)}(\hat{\mathbf{r}}) | \Psi_J \rangle|^2, \quad (21)$$

(where the energy differences, the speed of light, and the matrix elements in this formula are given in atomic units) The SI unit conversion factor is the inverse of the atomic unit of time $A_0 = 1/(2.418884326509 \times 10^{-17}) = 4.1341373336493 \times 10^{16}$ from the latest CODATA[33]. The results of our calculations are shown in Table II, where again we also indicate our agreement with the NIST database [30]. This level of agreement was again expected as we are using an infinite mass proton approximation when solving the two-body problem.

D. Calculation of dynamic dipole polarizabilities

The dynamic dipole ($k = 1$) polarizability for a state with angular momentum $j_I = \frac{1}{2}$ is independent of the magnetic projection m_I , whilst for $j_I > \frac{1}{2}$ it depends on m_I , i.e. via scalar ($\alpha_S^{(1)}$) and tensor ($\alpha_T^{(1)}$) components;

$$\alpha_I^{(1)}(\omega) = \alpha_S^{(1)}(\omega) + \left(\frac{3m_I^2 - j_I(j_I + 1)}{j_I(2j_I - 1)} \right) \alpha_T^{(1)}(\omega). \quad (22)$$

The 2^k -pole scalar polarizability is usually defined in terms of a sum over all intermediate states, excluding the initial state, whilst including the continuum [20],

$$\alpha_S^{(k)}(\omega) = \sum_{J \neq I}^N \frac{f_{IJ}^{(k)}}{\varepsilon_{IJ}^2 - \omega^2}. \quad (23)$$

The expression for the tensor part of the dipole polarizability for a state I can be written as

$$\begin{aligned} \alpha_T^{(1)}(\omega) &= 6 \sqrt{\frac{5j_I(2j_I - 1)(2j_I + 1)}{6(j_I + 1)(2j_I + 3)}} \\ &\times \sum_{J \neq I}^N (-1)^{j_I + j_J} \begin{Bmatrix} j_I & 1 & j_J \\ 1 & j_J & 2 \end{Bmatrix} \frac{f_{IJ}^{(1)}}{\varepsilon_{IJ}^2 - \omega^2}. \end{aligned} \quad (24)$$

Of interest is mapping out the locations of ‘tune-out’ wavelengths, ω_t (where $\alpha_I^{(1)}(\omega_t) \rightarrow 0$), and ‘magic’ wavelengths, ω_m (where $(\alpha_I^{(1)}(\omega_m) - \alpha_J^{(1)}(\omega_m)) \rightarrow 0$) [20].

1. Numerical test: polarizability of $Z = 60$ ion

A benchmark test of the calculation is to compute the static dipole polarizability of hydrogenic ion ground states. The static dipole polarizability of the hydrogenic ground state for $Z = 60$ (excluding negative energy states) is found to be 2.8024692×10^{-7} a.u.. This is in agreement to eight significant digits with a value computed recently using a B-spline basis [34]. The same level of agreement is achieved when negative energy states are included in the polarizability sum rule [34]. A similar degree of accuracy is achieved for the calculation of the quadrupole polarizability. The quadrupole polarizability of the hydrogenic ground state for $Z = 60$ (including negative energy states) is found to be $2.37114704 \times 10^{-10}$ a.u.. This is in agreement to eight significant digits with the B-spline value [34].

III. ATOMIC PROPERTIES OF Sr^+

Having independently validated the operation of our two codes, we now turn our attention to the computation of the challenging one-valence electron ion, Sr^+ , which requires the consequent usage of both codes. First we outline our treatment of the core-valence interaction.

A. Calculation of the core-valence interaction

The interaction of the valence electron with the core electrons can be approximated as a direct and exchange potential, along with a core-polarization interaction:

$$\hat{V}_{core} \approx \hat{V}_{dir} + \hat{V}_{exc} + \hat{V}_{p1}. \quad (25)$$

A detailed description of the relevant one-body matrix elements can be found in Ref. [2]. In brief, the matrix elements of the direct interaction can be written as,

$$\begin{aligned} & \langle \psi_{n_I} | V_{dir} | \psi_{n_J} \rangle \\ &= \delta_{\kappa_I, \kappa_J} \int_0^\infty \left(P_{n_I}(r) P_{n_J}(r) + Q_{n_I}(r) Q_{n_J}(r) \right) V_d(r) dr, \end{aligned} \quad (26)$$

where the direct core potential acts locally and radially,

$$V_d(r) = \int_0^r \frac{\rho_{core}(r')}{r} dr' + \int_r^\infty \frac{\rho_{core}(r')}{r'} dr'. \quad (27)$$

The ρ_{core} is the density of all of the core electrons, where

$$\rho_{core}(r) = \sum_{c=1}^{N_{core}} (2j_c + 1) (P_c^2(r) + Q_c^2(r)). \quad (28)$$

The N_{core} is the number of core orbitals (denoted by c) obtained from a preceding DF calculation (see Table I). The exchange matrix element between the i -th and j -th valence electron and the core electrons can be written as a sum over the interaction with each core electron, viz.

$$\begin{aligned} \langle \psi_i | V_{exc} | \psi_j \rangle &= -\delta_{\kappa_i, \kappa_j} \sum_{c=1}^{N_{core}} \sum_k (2j_c + 1) \\ &\times \left(\begin{array}{ccc} j_c & k & j_i \\ \frac{1}{2} & 0 & -\frac{1}{2} \end{array} \right)^2 R^k(c, i, j, c), \end{aligned} \quad (29)$$

where

$$\begin{aligned} R^k(a, b, c, d) &= \int_0^\infty \int_0^\infty (P_a(r_1) P_c(r_1) + Q_a(r_1) Q_c(r_1)) \\ &\times \frac{r_{<}^k}{r_{>}^{k+1}} (P_b(r_2) P_d(r_2) + Q_b(r_2) Q_d(r_2)) dr_1 dr_2. \end{aligned} \quad (30)$$

Here $r_{<}$ and $r_{>}$ are the lesser and greater of the distances r_1 and r_2 of the electrons respectively (one of which here is a core electron). The radial integrals are computed numerically using Gaussian integration [28], which enables the mixed usage of Slater-type orbitals (to most

TABLE III: The cutoff parameters, $\rho_{\ell j}$ of the core polarization potential, for an electron-Sr²⁺ interaction.

ℓ	j	$\rho_{\ell j} (a_0)$	j	$\rho_{\ell j} (a_0)$
s	$\frac{1}{2}$	2.04960	—	—
p	$\frac{1}{2}$	1.97169	$\frac{3}{2}$	1.97600
d	$\frac{3}{2}$	2.35353	$\frac{5}{2}$	2.36534
f	$\frac{5}{2}$	2.15023	$\frac{7}{2}$	2.19469

compactly represent the core) or Laguerre-type orbitals (which are orthogonal and thus be included towards completeness without linear dependence issues). In order to prevent the valence electrons collapsing into the core electron (S-spinor only) orbitals, a Gram-Schmidt orthogonalization of the orbital set is performed to ensure that all the electron orbitals are orthonormal.

B. Calculation of the semi-empirical potential

The e^- -Sr²⁺ one-body polarization potential V_{p1} is an extension of the semi-empirical polarization potential used previously [31], here including dipole, quadrupole, and octupole contributions as

$$V_{p1}(r) = - \sum_{k=1}^3 \frac{\alpha_{core}^{(k)}}{2r^{2(k+1)}} \sum_{\ell, j} g_{k, \ell, j}^2(r) |\ell, j\rangle \langle \ell, j|. \quad (31)$$

Here, the factors $\alpha_{core}^{(k)}$ is the static k -th order polarizability of the core electrons (obtained from independent calculations) and $g_{k, \ell, j}^2(r) = 1 - \exp(-r^{2(k+2)}/\rho_{\ell, j}^{2(k+2)})$ is a cutoff function designed to make the polarization potential finite at the origin, while we tune $\rho_{\ell, j}$ for each ℓ, j combination.

In our calculations, the core values adopted for the dipole is $\alpha_{core}^{(1)} = 5.813$ a.u. [6, 35], for the quadrupole is $\alpha_{core}^{(2)} = 17.15$ a.u. [6, 35], whilst for the octupole is $\alpha_{core}^{(3)} = 113$ a.u. [36]. The cut-off parameters for the polarization potentials are listed in Table III. These parameters are set by tuning to the energy of the lowest state of each (ℓ, j) symmetry to the experiment value. The dipole transition matrix elements were computed with a modified transition operator [4, 31, 37, 38], e.g.

$$\mathbf{r} = \mathbf{r} - \alpha_{core}^{(1)} \sqrt{1 - \exp(-r^6/\bar{\rho}^6)} \frac{\mathbf{r}}{r^3}. \quad (32)$$

The cutoff parameter $\bar{\rho}$ used in Eq. (32) was the average of the s , p and d cutoff parameters (note, the weighting of the s was doubled to give it same weighting as the two p and d orbitals).

1. Results: Energies of Sr^+

For the Sr^+ calculations we used Laguerre parameters $\lambda = 1.6$ for s orbitals and $\lambda = 1.2$ for the others, with $N = 50$ orbitals for each angular momentum. The energies for a number of low-lying states are given in Table IV. Comparing with the experimental data taken from the National Institute of Science and Technology (NIST) [30], we can find that the error of the present calculations (labeled as RCICP) is about 2×10^{-4} a.u. for the more highly excited s and p states while being about five times as large for the d states.

By tuning the polarization potential cutoff parameters, the spin-orbit splittings are correct for the $4d_j$ and $5p_j$ levels. This also makes reasonably accurate spin-orbit splittings for the more highly excited states. Such as, the present calculations of $6p_j$ splitting is 0.001315 a.u. while the experimental splitting is 0.001313 a.u.. The $5d_j$ RCICP splitting is 0.000406 a.u. while the experimental splitting is 0.000395 a.u..

C. Line strengths and lifetimes

The line strengths for a number of low-lying transitions of Sr^+ are listed in Table V. Line strengths are mainly given for dipole transitions, while the exceptions are of the $5s \rightarrow 4d_j$ transitions. Table V also gives the line strengths from a previous non-relativistic calculation [31], labeled as CICIP, which can be regarded as a precursor to the present calculation. Finally, Table V lists the line strengths of the relativistic all-order single and double many-body perturbation theory (MBPT-SD) calculation [36, 39].

The non-relativistic CICIP radial matrix elements are the same for the different members of the same spin-orbit doublets. So the different line strength are purely due to

TABLE IV: Theoretical (RCICP) and experimental energy levels (in Hartree) for some of the low-lying states of Sr^+ . The energies are given relative to the energy of the Sr^{2+} core. The experimental data are taken from the National Institute of Science and Technology (NIST) tabulation [30].

I	j	$\varepsilon(\text{RCICP})$	$\varepsilon(\text{Exp.})$	Δ_ε
5s	$\frac{1}{2}$	-0.4053555	-0.4053552	0.0000003
4d	$\frac{3}{2}$	-0.3390336	-0.3390336	0.0000000
	$\frac{5}{2}$	-0.3377563	-0.3377563	0.0000000
5p	$\frac{1}{2}$	-0.2973007	-0.2973008	0.0000001
	$\frac{3}{2}$	-0.2936464	-0.2936491	0.0000027
6s	$\frac{1}{2}$	-0.1875380	-0.1878515	0.0003135
5d	$\frac{3}{2}$	-0.1612581	-0.1625649	0.0013068
	$\frac{5}{2}$	-0.1608524	-0.1621700	0.0013176
6p	$\frac{1}{2}$	-0.1510966	-0.1512497	0.0001531
	$\frac{3}{2}$	-0.1497517	-0.1499367	0.0001850
4f	$\frac{7}{2}$	-0.1274645	-0.1274641	0.0000004
	$\frac{5}{2}$	-0.1274582	-0.1274582	0.0000000
7s	$\frac{1}{2}$	-0.1091774	-0.1093570	0.0001796
6d	$\frac{3}{2}$	-0.0969695	-0.0976983	0.0007288
	$\frac{5}{2}$	-0.0967790	-0.0975148	0.0007358
7p	$\frac{1}{2}$	-0.0923245	-0.0924291	0.0001046
	$\frac{3}{2}$	-0.0916778	-0.0918013	0.0001235
5f	$\frac{5}{2}$	-0.0815523	-0.0815557	0.0000034
	$\frac{7}{2}$	-0.0815463	-0.0815557	0.0000094
5g	$\frac{7}{2}$	-0.0802443	-0.0802252	0.0000191
	$\frac{9}{2}$	-0.0802442	-0.0802252	0.0000190

geometric factors related to the angular momentum of the states. The difference between the CICIP and present RCICP line strengths is typically small, not exceeding 6% for any of the strong transitions. Part of the differences that occur are due to the different energies of the spin-orbit doublets. The difference is about 0.1% for the resonance $5s \rightarrow 5p_j$ transitions. Differences can be larger for the weaker transitions with much smaller line strengths which are much more sensitive to small perturbations in the calculation of the matrix elements. The generally good agreement between the CICIP and RCICP matrix elements arises because both sets of calculations have their energies tuned to experimental values. The binding energy largely determines the long range part of the wavefunction and it is this part of the wavefunc-

TABLE V: Comparison of reduced electric dipole (E1) and quadrupole (E2) line strength for the principal transitions of Sr^+ with other calculations. The (x) notation indicates the error in the last digits.

Transition	RCICP	MBPT-SD [36, 39]	CICP [31]
Dipole			
$5s - 5p_{\frac{1}{2}}$	9.2852	9.474(111)	9.2729
$5s - 5p_{\frac{3}{2}}$	18.582	18.93(22)	18.546
$5s - 6p_{\frac{1}{2}}$	0.00203	0.00063(10)	0.000158
$5s - 6p_{\frac{3}{2}}$	0.000040	0.00116(29)	0.000315
$5p_{\frac{1}{2}} - 6s$	5.4819	5.434(65)	5.7963
$5p_{\frac{3}{2}} - 6s$	11.903	11.81(12)	11.593
$6s - 6p_{\frac{1}{2}}$	42.681	42.64(17)	42.414
$6s - 6p_{\frac{3}{2}}$	84.392	84.29(35)	84.827
$6p_{\frac{1}{2}} - 7s$	22.763	22.77(5)	23.964
$6p_{\frac{3}{2}} - 7s$	49.132	49.07(8)	47.928
$5p_{\frac{1}{2}} - 5d_{\frac{3}{2}}$	17.950	18.17(32)	18.724
$5p_{\frac{3}{2}} - 5d_{\frac{3}{2}}$	3.8161	3.869(59)	3.7448
$5p_{\frac{3}{2}} - 5d_{\frac{5}{2}}$	33.948	34.40(57)	33.703
$4d_{\frac{3}{2}} - 5p_{\frac{1}{2}}$	9.5873	9.685(181)	9.4865
$4d_{\frac{3}{2}} - 5p_{\frac{3}{2}}$	1.9005	1.910(36)	1.8973
$4d_{\frac{5}{2}} - 5p_{\frac{3}{2}}$	17.409	17.53(31)	17.076
$4d_{\frac{3}{2}} - 6p_{\frac{1}{2}}$	0.00121	0.00608(257)	0.00225
$4d_{\frac{3}{2}} - 6p_{\frac{3}{2}}$	0.00111	0.00260(76)	0.000449
$4d_{\frac{5}{2}} - 6p_{\frac{3}{2}}$	0.00757	0.00202(58)	0.00404
$4d_{\frac{3}{2}} - 4f_{\frac{5}{2}}$	8.5818	8.503(223)	8.6472
$4d_{\frac{5}{2}} - 4f_{\frac{5}{2}}$	0.6275	0.623(14)	0.6177
$4d_{\frac{5}{2}} - 4f_{\frac{7}{2}}$	12.543	12.45(30)	12.353
Quadrupole			
$5s - 4d_{\frac{3}{2}}$	123.04	123.94(87)	123.08
$5s - 4d_{\frac{5}{2}}$	187.50	188.98(140)	184.63

tion which dominates the calculation of the dipole and quadrupole matrix elements.

Our present RCICP calculations generally give improved results over our previous CICP calculations, as compared with the MBPT-SD line strengths shown in Table V. We now see agreement at the level of a couple of percent between most of the RCICP and MBPT-SD line strengths, and most of our results lie within their error estimates. The RCICP line strengths are 2% smaller than the MBPT-SD line strengths for the resonant $5s \rightarrow 5p_j$

transitions, although our results do lie outside their error estimates [36, 39]. The two most egregious cases are the weak $5s-6p_{\frac{1}{2}}$ and $4d_{\frac{5}{2}}-6p_{\frac{3}{2}}$ transitions where we are around 200% different, even with the relatively large MBPT-SD error estimates taken into account. All of the $> 2\%$ cases can be explained again due to the sensitivity to small perturbations in the calculations. The Sr^+ system presents an extreme benchmark challenge for all atomic structure methodologies.

Using the line strengths given in Table V, the lifetimes of $4d_j$ and $5p_j$ states can be easily obtained using Eqns. (21). Table VI gives the lifetimes of $4d_j$ states. The main contribution for the lifetimes of $4d_j$ comes from the E2 ($4d_j - 5s$) transitions. The underlying theoretical framework of the relativistic coupled cluster (RCC) and MBPT-SD approaches have many common features [14, 40, 41]. In many instances, however, atomic parameters computed using the RCC approach had significant differences with other independent calculations [42–45]. This situation is also prevalent for the lifetime of the $4d_j$ states. The RCC lifetime ratio 1.1933 is 8% larger than that given by either the RCICP and MBPT-SD calculations. The CICP lifetime ratio of 1.0965 is essentially due to the different energies of the two $4d_j$ states (since the matrix elements are the same in the CICP calculation). The RCICP lifetime ratio 1.1176 are in excellent agreement with the MBPT-SD ratio 1.1193 and most recent experiment ratio 1.115 [46].

TABLE VI: Lifetimes (τ in seconds) of the $4d_{\frac{3}{2}}$ and $4d_{\frac{5}{2}}$ levels of Sr^+ . The $4d_{\frac{3}{2}} : 4d_{\frac{5}{2}}$ lifetime ratio is also given.

Source	$\tau(4d_{\frac{3}{2}})$	$\tau(4d_{\frac{5}{2}})$	Ratio
RCICP	0.4442	0.3974	1.1176
RCC [47]	0.426(8)	0.357(12)	1.193(65)
CICP [31]	0.443	0.404	1.0965
MBPT-SD [39]	0.441(3)	0.394(3)	1.119(14)
Exp. [48]		0.372(25)	
Exp. [46]	0.455(29)	0.408(22)	1.115(139)
Exp. [49, 50]	0.435(4)	0.3908(16)	1.1131(68)

Different estimates of the $5p_j$ lifetimes are given in

Table VII. The $5p_j$ states have dipole transitions to two lower-lying states, namely the $5s$ and $4d_j$ states. The transition to the $5s$ state being about twenty times larger than the transition to the $4d_j$ states. The RCICP and MBPT-SD lifetimes differ by 2% and the most precise experimental estimates obtained from laser excitation of ion beams [51, 52] lie within the RCICP and MBPT-SD estimates. The RCC lifetimes are smaller than the RCICP and MBPT-SD results. The RCICP and MBPT-SD comparisons are reminiscent of the $4p_j$ lifetimes of Ca^+ . In Ca^+ one finds that the RCICP lifetime are about 2% larger than the MBPT-SD lifetimes [53]. The $5p_{\frac{1}{2}} : 5p_{\frac{3}{2}}$ lifetime ratio agrees very well with experiment for both calculations.

D. Static Polarizabilities

The contributions from the core to the dynamic polarizabilities is only via a scalar contribution, which was included by a pseudo-oscillator strength distribution [6, 55, 56],

$$\alpha_S^{(core)}(\omega) = \sum_i^{N_C} \frac{f_i^{(1)}}{\varepsilon_i^2 - \omega^2}. \quad (33)$$

The pseudo-oscillator strength distribution is tabulated in Table VIII, using the number of electrons in each shell as the oscillator strength. Note that in the calculations of polarizability difference for any two states, the core polarizabilities will effectively cancel each other.

The static dipole and quadrupole polarizabilities of the $5s$, $5p_j$ and $4d_j$ states are given in Table IX. Once again the overall agreement for the dipole polarizability between the RCICP and MBPT-SD calculations is at the level of 1 – 2%. The present calculations also agree with the all-order relativistic coupled cluster method with the singles and doubles approximation (RCC all-order) results. The RCICP ground state dipole polarizability of 90.1 a.u. is about 2% smaller than the MBPT-SD polarizability. This is the direct consequence of the slightly different line strengths for the resonant transition. Since the energies of the lowest eigenstates have been tuned to the experimental values in both calculations while the

slightly higher difference in the energies of the other excited states has a negligible effect on the polarizability. There is only one experimental Sr^+ dipole polarizability that has been obtained [57]. In that experiment, the energy differences between the $5snf$, $5sng$, $5snh$ and $5sni$ states of neutral strontium have been used to make an estimate of the Sr^+ core polarizability. However, the relatively large uncertainty of 13% cannot be used to discriminate between the different theoretical estimates.

The RCICP quadrupole polarizability of the ground state is about 1% smaller than the MBPT-SD polarizability. The non-relativistic CICP calculation is 2% smaller than the MBPT-SD polarizability. This difference is a direct consequence of the difference in the underlying line strengths between the various calculations.

The RCICP dipole polarizabilities of $5p_j$ agree with MBPT-SD polarizability very well. The dipole polarizability of $5p_j$ states are negative. That is because the downward transition from $5p_j$ to the $5s$ and $4d_j$ have very big negative oscillator strengths which results in the negative polarizability. This is evident in Table XI (and Supplemental Tables IV and V), shows the contributions from different transitions on the polarizabilities. The tensor dipole polarizability of $5p_{\frac{3}{2}}$ of RCICP calculations is 8% smaller than the MBPT-SD calculations. That is mainly because the matrix element of $5s \rightarrow 5p_{\frac{3}{2}}$ of RCICP is smaller than the MBPT-SD matrix element. The RCICP dipole scalar and tensor polarizabilities of $4d_j$ states agree with MBPT-SD and RCC polarizabilities very well.

One important application of polarizability is to give the magic wavelength by setting the difference between the polarizabilities of the involved two eigenstates to be zero. As an example, Table X gives the difference of static dipole polarizabilities for the $5s$ and $4d_j$ states. The polarizability difference between the $5s$ and $4d_{\frac{5}{2}}$ is relevant to the determination of the error budget for the $5s \rightarrow 4d_{\frac{5}{2}}$ clock transition [23]. Until recently, the only estimates of the polarizability difference came from atomic structure calculations [31, 39, 59, 60]. However, the scalar polarizability for this transition has recently been measured by utilizing the time-dilation effect [22]. The time di-

TABLE VII: Lifetimes (τ in nanoseconds) of the $5p_{\frac{1}{2}}$ and $5p_{\frac{3}{2}}$ states. The $5p_{\frac{1}{2}} : 5p_{\frac{3}{2}}$ lifetime ratio is also given. The quantity R gives fraction of the total decay rate arising from the indicated transition.

Level	RCICP	MBPT-SD [39]	RCC[54]	Exp. [51]	Exp. [52]
$\tau(5p_{\frac{1}{2}})$	7.523	7.376	7.16	7.47(7)	7.39(7)
$R(5p_{\frac{1}{2}} - 5s_{\frac{1}{2}})$	0.9439	0.9444	0.9338		
$R(5p_{\frac{1}{2}} - 4d_{\frac{1}{2}})$	0.0562	0.0556	0.0662		
$\tau(5p_{\frac{3}{2}})$	6.773	6.653	6.44	6.69(7)	6.63(7)
$R(5p_{\frac{3}{2}} - 5s_{\frac{1}{2}})$	0.9394	0.9400	0.9287		
$R(5p_{\frac{3}{2}} - 4d_{\frac{3}{2}})$	0.0064	0.0064	0.0075		
$R(5p_{\frac{3}{2}} - 4d_{\frac{5}{2}})$	0.0542	0.0536	0.0637		
$5p_{\frac{1}{2}} : 5p_{\frac{3}{2}}$ Ratio	1.111	1.109	1.111	1.117(20)	1.114(20)

TABLE VIII: Pseudospectral oscillator strength distribution for the Sr^{2+} core. Energies are given in a.u..

i	orbital	ε_i	f_i
1	$1s^2$	583.696	2
2	$2s^2$	80.400	2
3	$2p^6$	73.005	6
4	$3s^2$	13.484	2
5	$3p^6$	10.709	6
6	$3d^{10}$	5.703	10
7	$4s^2$	1.906	2
8	$4p^6$	1.108	6

lation experiment gives a scalar polarizability difference that lies almost exactly halfway between the RCICP and MBPT-SD polarizability differences.

E. Dynamic polarizabilities and magic wavelengths

The Sr^+ dipole scalar and tensor dynamic polarizabilities are computed here as per Eqn. 22, including the core contribution as per Eqn. 33. The magic wavelength is calculated by setting the dynamical polarizability difference between the two involved eigenstates to be zero. An example breakdown for the $5s_{\frac{1}{2}}$ and $5p_{\frac{1}{2}}$ polarizabilities are given for both for the static case ($\omega = 0$) and also at the first magic wavelength $\omega = 0.05961933$ a.u. in Table XI.

The dynamic polarizabilities of the $5s_{\frac{1}{2}}$ and $5p_{\frac{1}{2}}$ states

of Sr^+ are shown in Fig. 2(a). Note that these calculations assume linearly-polarized light. The only magic wavelength for this transition for wavelengths greater than 400 nm occurs at $\lambda = 764.238$ nm ($\omega = 0.05961933$ a.u.). This occurs when the photon energy exceeds the energy for the $5p_{\frac{1}{2}}-4d_{\frac{3}{2}}$ transition. While the $5s_{\frac{1}{2}}$ polarizability is dominated by $5s_{\frac{1}{2}} - 5p_j$ transition. The breakdown of the $5p_{\frac{1}{2}}$ polarizability tabulated in Table XI reveals that the transitions to the $5s$, $6s$, $4d_{\frac{3}{2}}$ and $5d_{\frac{3}{2}}$ states all make significant contributions to the $5p_{\frac{1}{2}}$ polarizability.

The dynamic polarizabilities of the $5s_{\frac{1}{2}}$ and $5p_{\frac{3}{2}}$ states of Sr^+ are in Fig. 2(b). Supplemental Tables IV and V list the breakdown of the polarizabilities for the static case and at the magic wavelengths for both m_j -values. There are seven magic wavelengths below $\omega = 0.110$ a.u. and four below 0.070 a.u.. Supplemental Tables IV and V reveals that the position of the magic wavelengths near 1004 nm and 1009 nm are strongly influenced by the relative sizes of the $5p_{\frac{3}{2}} \rightarrow 4d_{\frac{3}{2}}$ and $5p_{\frac{3}{2}} \rightarrow 4d_{\frac{5}{2}}$ line strengths. These two magic wavelengths occur when the photon energy lie between the transition energies of $5p_{\frac{3}{2}} \rightarrow 4d_{\frac{3}{2}}$ and $5p_{\frac{3}{2}} \rightarrow 4d_{\frac{5}{2}}$. Transitions to the $ns_{\frac{1}{2}}$ states make no contribution to the $5p_{\frac{3}{2},m=\frac{3}{2}}$ state polarizability for linearly polarized light. Combining with the experimental matrix elements of $5s \rightarrow 5p_j$ transitions, the measurement of 1009 nm magic wavelength could be able to determine the oscillator strength ratio of $f_{5p_{\frac{3}{2}} \rightarrow 4d_{\frac{3}{2}}} : f_{5p_{\frac{3}{2}} \rightarrow 4d_{\frac{5}{2}}}$. Suppose that all the re-

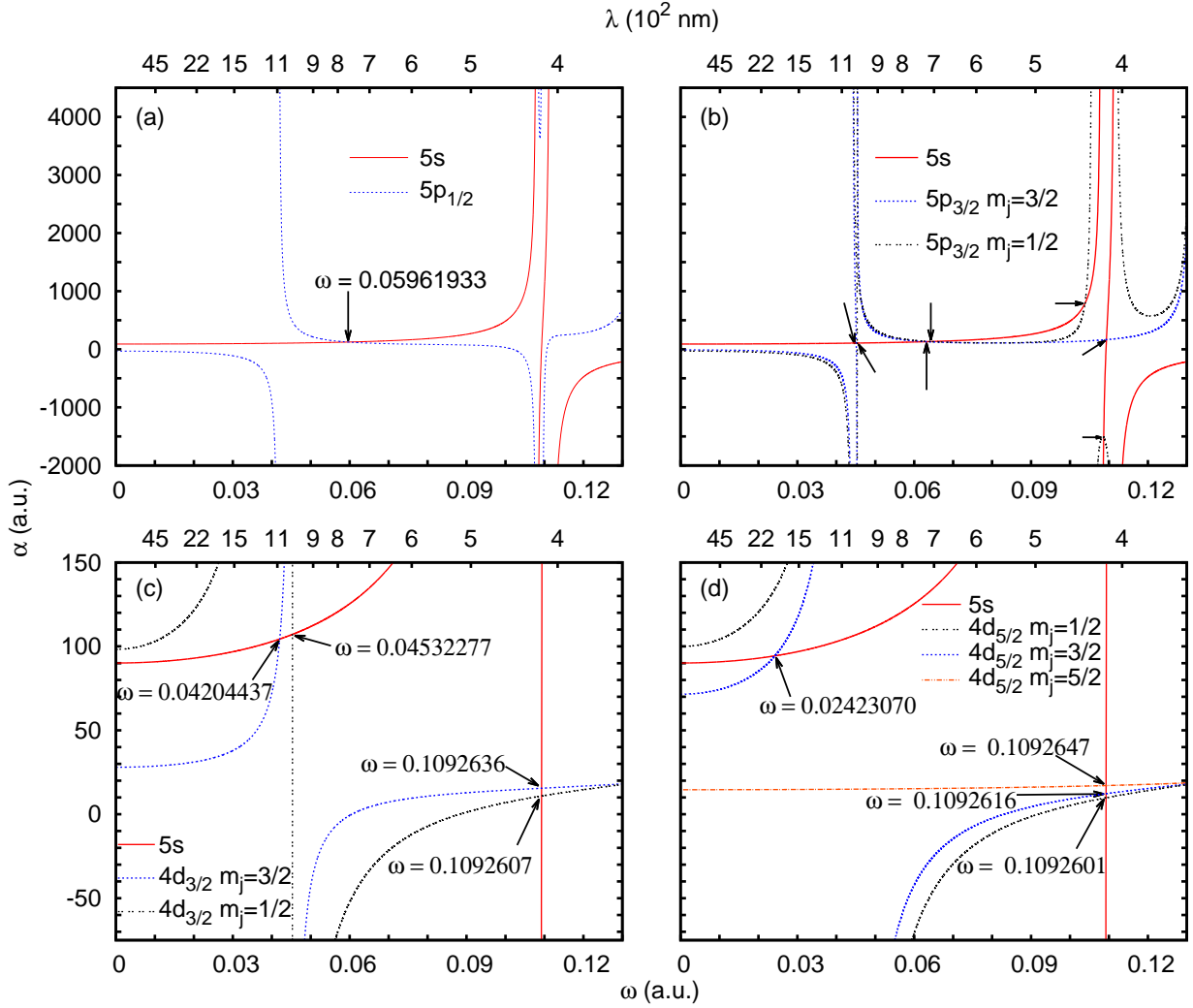


FIG. 2: (color online) Dynamic polarizabilities of various states of Sr^+ . Panel (a) compares the $5s_{\frac{1}{2}}$ and $5p_{\frac{1}{2}}$ states, (b) compares $5s_{\frac{1}{2}}$ and $5p_{\frac{3}{2}}$, (c) compares $5s_{\frac{1}{2}}$ and $4d_{\frac{3}{2}}$, (d) compares $5s_{\frac{1}{2}}$ and $4d_{\frac{5}{2}}$. The various magic wavelengths between the respective states are identified by arrows.

maining components of $5p_{\frac{3}{2}}$ polarizability including the $5p_{\frac{3}{2}} \rightarrow 5d_j$ contributions is 5%. Then the overall uncertainty to the polarizability is less than 1%.

There are several other magic wavelengths that are worth mentioning. The magic wavelengths near 709 nm and 721 nm are caused by the gradual increase of the $5s_{\frac{1}{2}}$ polarizability as the photon energy approaches the $5s \rightarrow 5p_j$ excitation energy and the gradual decrease of the $5p_{\frac{3}{2}}$ polarizability as the energy becomes increasingly distant from the $5p_{\frac{3}{2}} \rightarrow 4d_j$ transition energy. The magic wavelength at 438 nm for the $5p_{\frac{3}{2}, m=\frac{1}{2}}$ magnetic sub-level is triggered by the polarizability associated with

the $5p_{\frac{3}{2}} \rightarrow 6s$ transition. The magic wavelengths near 416 nm and 419 nm are caused by the rapid variation of the $5s$ polarizability for a photon energy lying between the excitation energies from $5s$ to $5p_{\frac{1}{2}}$ and $5p_{\frac{3}{2}}$ states. These magic wavelengths can give an estimate of the contribution to the $5p_{\frac{3}{2}}$ polarizability arising from excitations to the nd_j levels.

The dynamic polarizabilities of the $5s$ and $4d_{\frac{5}{2}}$ states are shown in Fig. 2(d) while Supplemental Table VI lists the breakdown of the polarizabilities for the static case and at the magic wavelengths. This is probably the most interesting transition since it is the transition of

TABLE IX: Static ($\omega = 0$) scalar and tensor dipole polarizabilities, $\alpha_S^{(1)}$ and $\alpha_T^{(1)}$, and static quadrupole polarizabilities $\alpha_S^{(2)}$ for low-lying states of the Sr^+ ion. All numbers are given in a.u..

State	term	RCICP	Others	Others Ref.
$5s_{\frac{1}{2}}$	$\alpha_S^{(1)}$	90.10	92.2(7)	MBPT-SD [36]
			91.30	MBPT-SD [39]
			90.54	RCC all-order [58]
			88.29	RCC [59]
			89.88	CICP [31]
			86(11)	Expt. [57]
$5p_{\frac{1}{2}}$	$\alpha_S^{(2)}$	1356.27	1370.0(28)	MBPT-SD [36]
			1346	CICP [31]
$5p_{\frac{3}{2}}$	$\alpha_S^{(1)}$	-31.29	-32.2(9)	MBPT-SD [36]
			-31.27	RCC all-order [58]
$5p_{\frac{3}{2}}$	$\alpha_S^{(2)}$	31595.9	-21.4(8)	MBPT-SD [36]
			-20.97	RCC all-order [58]
$4d_{\frac{3}{2}}$	$\alpha_T^{(1)}$	9.836	10.74(23)	MBPT-SD [36]
			10.52	RCC all-order [58]
$4d_{\frac{3}{2}}$	$\alpha_S^{(2)}$	-13098.8	63.3(9)	MBPT-SD [36]
			63.74	RCC all-order [58]
$4d_{\frac{5}{2}}$	$\alpha_S^{(1)}$	61.99	61.43(52)	RCC [59]
			62.08	RCC all-order [58]
$4d_{\frac{5}{2}}$	$\alpha_T^{(1)}$	-47.38	-35.5(6)	MBPT-SD [36]
			-35.26	RCC all-order [58]
$4d_{\frac{5}{2}}$	$\alpha_S^{(2)}$	2713.8	-35.42(25)	RCC [59]
			62.87(75)	RCC [59]
$4d_{\frac{5}{2}}$	$\alpha_T^{(1)}$	-47.38	-47.7(8)	MBPT-SD [36]
			-47.35	RCC all-order [58]
$4d_{\frac{5}{2}}$	$\alpha_S^{(2)}$	-1728.3	-48.83(25)	RCC [59]

the Sr^+ optical frequency standard. This transition has one magic wavelength at 1880 nm. This is caused by the increase in the $4d_{\frac{5}{2}, m=\frac{3}{2}}$ polarizability as the photon energy approaches the $4d_{\frac{5}{2}} \rightarrow 5p_{\frac{3}{2}}$ excitation energy. The other three magic wavelengths lie close to 417 nm and are all caused by the rapid change of the $5s$ polarizability for photon energies lying between the excitation thresh-

TABLE X: Difference of static dipole polarizabilities (in a.u.) for the $5s - 4d_j$ transitions of the Sr^+ ion.

Method	$5s - 4d_{\frac{5}{2}}$	$5s - 4d_{\frac{3}{2}}$
RCICP	28.11	27.00
MBPT-SD [36]	30.2	28.9
RCC all-order [58]	28.46	26.8
RCC [59]	25.4	26.9
Expt. [22]	29.075(43)	

TABLE XI: The contributions of individual transitions to the polarizabilities (in a.u.) of the $5s_{\frac{1}{2}}$ and $5p_{\frac{1}{2}}$ states for the static case and at the magic wavelengths. These results assume linearly-polarized light. $\delta\lambda$ are uncertainties calculated by assuming certain matrix elements have $\pm 2\%$ uncertainties.

ω (a.u.)	0	0.05961933
λ (nm)	∞	764.2378
$\delta\lambda$ (nm)		8
Ref. [58] (nm)		769.44
	$5s_{\frac{1}{2}}$	
$5p_{\frac{1}{2}}$	28.6439	41.1806
$5p_{\frac{3}{2}}$	55.4498	77.5362
Remainder	0.1891	0.1918
Core	5.8128	5.8276
Total	90.0957	124.7362
	$5p_{\frac{1}{2}}$	
$5s_{\frac{1}{2}}$	-28.6439	-41.1806
$4d_{\frac{3}{2}}$	-76.5768	73.5687
$6s_{\frac{1}{2}}$	16.6954	23.7393
$5d_{\frac{3}{2}}$	44.4075	55.2192
Remainder	7.0082	7.5619
Core	5.8128	5.8276
Total	-31.2969	124.7362

olds of the $5p_j$ doublet. The magic wavelength mainly arises from the cancellation of the $5p_{\frac{1}{2}}$ and $5p_{\frac{3}{2}}$ contributions to the $5s$ dynamic polarizability. These three magic wavelengths would allow a determination of the oscillator strength ratio of $f_{5s \rightarrow 5p_{\frac{1}{2}}} : f_{5s \rightarrow 5p_{\frac{3}{2}}}$. This is similar to Ca^+ [53, 61], in which the magic wavelength of $3d_{\frac{5}{2}} \rightarrow 4s_{\frac{1}{2}}$ clock transition lying between the transition wavelengths of the $4s \rightarrow 4p_j$ doublet was measured and

the ratio of the oscillator strengths $f_{4s \rightarrow 4p_{\frac{1}{2}}} : f_{4s \rightarrow 4p_{\frac{3}{2}}}$ were determined with a deviation of less than 0.5%.

The dynamic polarizabilities of the $5s$ and $4d_{\frac{3}{2}}$ states are shown in Fig. 2(c) while Supplemental Table VII lists the breakdown of the polarizabilities for the static case and at the magic wavelengths. This transition has one magic wavelength at 1082 nm. This is caused by the increase in the $4d_{\frac{3}{2}, m=\frac{3}{2}}$ polarizability as the photon energy approaches the $4d_{\frac{3}{2}} \rightarrow 5p_{\frac{3}{2}}$ excitation energy. Another magic wavelength (1005 nm) occurs at a slightly higher photon energy. It is caused by the rapid change of the $4d_{\frac{3}{2}}$ polarizability for photon energies lying between the excitation energies of the $4d_{\frac{3}{2}} \rightarrow 5p_j$ doublet. Combining with the experimental results of $5s \rightarrow 5p_j$ oscillator strength, measurement of this magic wavelength would give an estimate of the oscillator strength ratio for $f_{4d_{\frac{3}{2}} \rightarrow 5p_{\frac{1}{2}}} : f_{4d_{\frac{3}{2}} \rightarrow 5p_{\frac{3}{2}}}$.

The other two magic wavelengths lie close to 417 nm are all caused by the rapid change of the $5s$ polarizability for photon energies lying between the excitation thresholds of the $5s \rightarrow 5p_j$ doublet. Like the magic wavelength near 417 nm for clock transition $5s \rightarrow 5d_{\frac{5}{2}}$, measurement of these two magic wavelengths would also allow a determination of the oscillator strength ratio for the $5s \rightarrow 5p_{\frac{1}{2}}$ and $5s \rightarrow 5p_{\frac{3}{2}}$ transition.

F. Uncertainties in the magic wavelength positions

An uncertainty analysis has been done for the magic wavelengths given in the preceding section. This analysis estimates how uncertainties in the matrix elements will translate into changes in the magic wavelengths. The motivation for this analysis is to define reasonable upper and lower limits on the wavelength to assist an experimental search for these magic wavelengths.

For the $5s \rightarrow 5p_j$ polarizability differences, the matrix elements of $5s \rightarrow 5p_j$, $5p_j \rightarrow 5s$, $5p_j \rightarrow 4d_j$, $5p_j \rightarrow 6s$ and $5p_j \rightarrow 5d_j$ are dominant. For the $5s \rightarrow 4d_j$ polarizability differences, the $5s \rightarrow 5p_j$ and $4d_j \rightarrow 5p_j$ matrix elements are dominant. All these matrix elements were changed by 2% (as most of the reliable calculations and

experiments agree with each other within a 2% difference) and the magic wavelengths were recomputed. The resultant difference is set as the uncertainty of the magic wavelength. The matrix elements involving the different spin-orbit states of the same multiplet were all given the same scaling.

The uncertainties of each magic wavelength is given in Table XI (and Supplemental Tables IV, V, VI and VII). It can be found that the magic wavelengths 764 nm for $5s \rightarrow 5p_{\frac{1}{2}}$, 709 nm for $5s \rightarrow 5p_{\frac{3}{2}, m=\frac{1}{2}}$, 721 nm for $5s \rightarrow 5p_{\frac{3}{2}, m=\frac{3}{2}}$, 1083 nm for $5s \rightarrow 4d_{\frac{3}{2}, m=\frac{3}{2}}$, and 1880 nm for $5s \rightarrow 4d_{\frac{5}{2}, m=\frac{3}{2}}$ are relatively sensitive to change in the matrix element. The uncertainties of magic wavelength are from 4 nm to 133 nm. The reason is that the rate of change of $5s$ and $5p_j$ (or $4d_j$) polarizabilities are small near these magic wavelength, namely $d\alpha/d\omega$ are small. The magic wavelength calculated by Kaur *et al.* [58] using RCC all-order method lie in our uncertainties.

There are some of the magic wavelengths, however, such as 1009 nm, 1004 nm, and 417 nm, that are relatively insensitive to the changes of matrix elements. The magic wavelength 1009 nm, 1004 nm lie in between the transition energy of $5p_{\frac{3}{2}} \rightarrow 4d_j$ spin-orbit doublet. The magic wave lengths near the 417 nm lie between the transition energy of $5s \rightarrow 5p_j$ spin-orbit doublet. Present calculations of magic wavelengths agree with RCC all-order results of Kaur *et al.* [58] excellently.

Experimental determination of the oscillator strengths for the resonant $5s \rightarrow 5p_j$ transitions using a lifetime approach is complicated due to the existence of the $4d_j \rightarrow 5p_j$ transitions. However, the measurement of magic wavelengths near 417 nm for the $5s \rightarrow 4d_j$ transitions can give a reasonable estimate of the oscillator ratio of the two transitions of the $5s \rightarrow 5p_j$ doublet since the polarizability of the $5s$ state is so much larger than any of the other polarizabilities. The magic wavelength at 416.9999 nm changes by 0.0002 nm when the $4d_{\frac{5}{2}} - 4f_j$ matrix elements are changed by 2%.

IV. CONCLUSION

The development and realization of a relativistic model potential description of quasi single electron atoms and ions was presented. Rather than using a B-spline basis [62], the single electron spinors are expanded as a linear combination of S-spinors and L-spinors. The starting point of the calculation is a DF calculation for the core state. The DF wavefunctions then serve as a starting point for the calculations to describe the ground and excited states of quasi single electron atoms or ions. The core electrons are kept frozen, where the direct and exchange interactions between the valence electron and the core are computed without approximation. Dynamical interactions between the valence electron and the core beyond the DF level are incorporated through semi-empirical polarization potentials.

The method was applied to the description of the low-lying states of Sr^+ giving line strengths and polarizabilities that are generally within 1 – 2% of the significantly more computationally demanding relativistic all-order singles and doubles method [36, 39]. A number of magic wavelengths are identified for the $5s \rightarrow 5p_{\frac{1}{2}}$, $5s \rightarrow 5p_{\frac{3}{2}}$, $5s \rightarrow 4d_{\frac{3}{2}}$ and $5s \rightarrow 4d_{\frac{5}{2}}$ transitions. We recommend that the measurements of 1009 nm magic wavelength for the $5s \rightarrow 5p_{\frac{3}{2}}$ transition could be able to determine the oscillator strength ratio of $f_{5p_{\frac{3}{2}} \rightarrow 4d_{\frac{3}{2}}} : f_{5p_{\frac{3}{2}} \rightarrow 4d_{\frac{5}{2}}}$. The de-

termination of the magic wavelengths for the $5s \rightarrow 4d_{\frac{3}{2}}$ and $5s \rightarrow 4d_{\frac{5}{2}}$ transitions near 417 nm would allow a determination of the oscillator strength ratio for the $5s \rightarrow 5p_{\frac{1}{2}}$ and $5s \rightarrow 5p_{\frac{3}{2}}$ transitions.

This approach can also be used for a variety of heavy atoms or ions, such as Cs, Ba^+ , Yb^+ , and so on. Atomic properties including the energy levels, the oscillator strengths, the static and dynamic multipole polarizabilities, the black-body radiation shifts, and the dispersion coefficients that characterize the long-range interaction between pairs of atoms, can be studied with improved accuracy over our previous non-relativistic-based CICP treatment [6].

Acknowledgments

This research was partially supported by the Australian Research Council (ARC) Discovery Project DP1092620. The work of JJ was supported by National Natural Science Foundation of China (NSFC) (Grants No.11147018 and 11564036) and YC was supported by NSFC (Grants No.11304063). The work of MWJB was supported by an ARC Future Fellowship (FT100100905). The authors would like to thank Prof. Ulyana Safronova for providing tables of reduced matrix elements for Sr^+ . We would like to thank Prof. Fumihiro Koike for his valuable suggestions.

-
- [1] H. M. Quiney, I. P. Grant, and S. Wilson, *J. Phys. B* **22**, L15 (1989), URL <http://dx.doi.org/10.1088/0953-4075/22/2/001>.
- [2] I. P. Grant and H. M. Quiney, *Phys. Rev. A* **62**, 022508 (2000), URL <http://dx.doi.org/10.1103/PhysRevA.62.022508>.
- [3] I. P. Grant, *Relativistic Quantum Theory of Atoms and Molecules Theory and Computation* (Springer, New York, 2007), URL <http://dx.doi.org/10.1007/978-0-387-35069-1>.
- [4] J. Mitroy, D. C. Griffin, D. W. Norcross, and M. S. Pindzola, *Phys. Rev. A* **38**, 3339 (1988), URL <http://dx.doi.org/10.1103/PhysRevA.38.3339>.
- [5] J. Mitroy, *J. Phys. B* **26**, 3703 (1993), URL <http://dx.doi.org/10.1088/0953-4075/26/21/009>.
- [6] J. Mitroy and M. W. J. Bromley, *Phys. Rev. A* **68**, 052714 (2003), URL <http://dx.doi.org/10.1103/PhysRevA.68.052714>.
- [7] J. Migdalek and W. E. Baylis, *J. Phys. B* **11**, L497 (1978), URL <http://dx.doi.org/10.1088/0022-3700/11/17/001>.
- [8] J. Mitroy, *Phys. Rev. A* **78**, 052515 (2008), URL <http://dx.doi.org/10.1103/PhysRevA.78.052515>.
- [9] S. R. Lundeen, *Adv. At. Mol. Opt. Phys.* **52**, 161 (2005), URL [http://dx.doi.org/10.1016/S1049-250X\(05\)52004-4](http://dx.doi.org/10.1016/S1049-250X(05)52004-4).
- [10] R. A. Komara, M. A. Gearba, C. W. Fehrenbach, and S. R. Lundeen, *J. Phys. B* **38**, S87 (2005), URL <http://dx.doi.org/10.1088/0953-4075/38/S1/001>.

- <http://dx.doi.org/10.1088/0953-4075/38/2/007>.
- [11] M. S. Safronova, S. G. Porsev, M. G. Kozlov, and C. W. Clark, *Phys. Rev. A* **85**, 052506 (2012), URL <http://dx.doi.org/10.1103/PhysRevA.85.052506>.
- [12] J. Mitroy and M. S. Safronova, *Phys. Rev. A* **79**, 012513 (2009), URL <http://dx.doi.org/10.1103/PhysRevA.79.012513>.
- [13] M. S. Safronova, M. G. Kozlov, and C. W. Clark, *Phys. Rev. Lett.* **107**, 143006 (2011).
- [14] S. G. Porsev, M. S. Safronova, and M. G. Kozlov, *Phys. Rev.* **85**, 062517 (2012), 1203.4169.
- [15] J. Migdalek and W. E. Baylis, *J. Phys. B* **17**, L459 (1984).
- [16] J. Migdalek and W. E. Baylis, *J. Phys. B* **19**, 1 (1986).
- [17] J. Migdalek and W. E. Baylis, *Z. Phys. D* **27**, 9 (1993).
- [18] J. Migdalek and A. Glowacz-Proszkiewicz, *J. Phys. B* **40**, 4143 (2007).
- [19] J. Migdalek, *Can. J. Phys.* **54**, 118 (1976), URL <http://dx.doi.org/10.1139/p76-014>.
- [20] J. Mitroy, M. S. Safronova, and C. W. Clark, *J. Phys. B* **43**, 202001 (2010), URL <http://dx.doi.org/10.1088/0953-4075/43/20/202001>.
- [21] J. Mitroy, *Aust. J. Phys.* **52**, 973 (1999), URL <http://dx.doi.org/10.1071/PH99042>.
- [22] P. Dubé, A. A. Madej, M. Tibbo, and J. E. Bernard, *Phys. Rev. Lett.* **112**, 173002 (2014), URL <http://link.aps.org/doi/10.1103/PhysRevLett.112.173002>.
- [23] A. A. Madej, P. Dubé, Z. Zhou, J. E. Bernard, and M. Gertszvolf, *Phys. Rev. Lett.* **109**, 203002 (2012).
- [24] A. D. Ludlow, M. M. Boyd, J. Ye, E. Peik, and P. O. Schmidt, *Rev. Mod. Phys.* **87**, 637 (2015), URL <http://dx.doi.org/10.1103/RevModPhys.87.637>.
- [25] S. Kaneko, *J. Phys. B* **10**, 3347 (1977).
- [26] E. Clementi and C. Roetti, *At. Data Nucl. Data Tables* **14**, 177 (1974).
- [27] F. A. Parpia, C. Froese Fischer, and I. P. Grant, *Comp. Phys. Commun.* **94**, 249 (1996).
- [28] M. W. J. Bromley and J. Mitroy, *Phys. Rev. A* **65**, 012505 (2001), URL <http://dx.doi.org/10.1103/PhysRevA.65.012505>.
- [29] M. Abramowitz and I. E. Stegun, eds., *Handbook of Mathematical Functions* (US GPO, Washington DC, 1972), Natl. Bur. Stand. Appl. Math. Ser. 55.
- [30] A. Kramida, Y. Ralchenko, J. Reader, and NIST ASD Team, *NIST Atomic Spectra Database (v5.0.0)* (2012), URL <http://physics.nist.gov/asd>.
- [31] J. Mitroy, J. Y. Zhang, and M. W. J. Bromley, *Phys. Rev. A* **77**, 032512 (2008), URL <http://dx.doi.org/10.1103/PhysRevA.77.032512>.
- [32] D. E. Kelleher and L. I. Podobedova, *J. Phys. Chem. Ref. Data* **37**, 267 (2008).
- [33] P. J. Mohr, D. B. Newell, and B. N. Taylor, ArXiv e-prints (2015), 1507.07956.
- [34] L. Y. Tang, Y. H. Zhang, X. Z. Zhang, J. Jiang, and J. Mitroy, *Phys. Rev. A* **86**, 012505 (2012).
- [35] W. R. Johnson, D. Kolb, and K. Huang, *At. Data Nucl. Data Tables* **28**, 333 (1983).
- [36] U. I. Safronova, *Phys. Rev. A* **82**, 022504 (2010), URL <http://link.aps.org/doi/10.1103/PhysRevA.82.022504>.
- [37] S. Hameed, A. Herzenberg, and M. G. James, *J. Phys. B* **1**, 822 (1968).
- [38] S. Hameed, *J. Phys. B* **5**, 746 (1972).
- [39] D. Jiang, B. Arora, M. S. Safronova, and C. W. Clark, *J. Phys. B* **42**, 154020 (2009).
- [40] R. Pal, M. S. Safronova, W. R. Johnson, A. Derevianko, and S. G. Porsev, *Phys. Rev. A* **75**, 042515 (2007).
- [41] M. S. Safronova and W. R. Johnson, *Adv. At. Mol. Opt. Phys.* **55**, 191 (2008).
- [42] L. W. Wansbeek, B. K. Sahoo, R. G. E. Timmermans, B. P. Das, and D. Mukherjee, *Phys. Rev. A* **78**, 012515 (2008).
- [43] L. W. Wansbeek, B. K. Sahoo, R. G. E. Timmermans, B. P. Das, and D. Mukherjee, *Phys. Rev. A* **82**, 029901(E) (2010).
- [44] M. S. Safronova and U. I. Safronova, *Phys. Rev. A* **83**, 012503 (2011).
- [45] J. Mitroy, J. Y. Zhang, and K. Varga, *Phys. Rev. Lett.* **101**, 123201 (2008), URL <http://dx.doi.org/10.1103/PhysRevLett.101.123201>.
- [46] E. Biémont, J. Lidberg, S. Mannervik, L.-O. Norlin, P. Royen, A. Schmitt, W. Shi, and X. Tordoir, *Eur. Phys. J. D* **11**, 355 (2000), URL <http://dx.doi.org/10.1007/s100530070063>.
- [47] B. K. Sahoo, M. R. Islam, B. P. Das, R. K. Chaudhuri, and D. Mukherjee, *Phys. Rev. A* **74**, 062504 (2006).
- [48] A. A. Madej and J. D. Sankey, *Opt. Lett.* **15**, 634 (1990).
- [49] S. Mannervik, J. Lidberg, L.-O. Norlin, P. Royen, A. Schmitt, W. Shi, and X. Tordoir, *Phys. Rev. Lett.* **83**, 698 (1999).
- [50] V. Letchumanan, M. A. Wilson, P. Gill, and A. G. Sinclair, *Phys. Rev. A* **72**, 012509 (2005).
- [51] P. Kuske, N. Kirchner, W. Wittmann, H. J. Andra, and

- D. Kaiser, Phys. Lett. **64A**, 377 (1978).
- [52] E. H. Pinnington, R. W. Berends, and M. Lumsden, J. Phys. B **28**, 2095 (1995).
- [53] L. Y. Tang, M. W. J. Bromley, Z. C. Yan, and J. Mitroy, Phys. Rev. A **87**, 032507 (2013), URL <http://dx.doi.org/10.1103/PhysRevA.87.012509>.
- [54] J. Kaur, D. K. Nandy, B. Arora, and B. K. Sahoo, Phys. Rev. A **91**, 012705 (2015), URL <http://link.aps.org/doi/10.1103/PhysRevA.91.012705>.
- [55] D. J. Margoliash and W. J. Meath, J. Chem. Phys. **68**, 1426 (1978).
- [56] A. Kumar and W. J. Meath, Mol. Phys. **54**, 823 (1985).
- [57] J. Nunkaew, E. S. Shuman, and T. F. Gallagher, Phys. Rev. A **79**, 054501 (2009), URL <http://link.aps.org/doi/10.1103/PhysRevA.79.054501>.
- [58] J. Kaur, S. Singh, B. Arora, and B. K. Sahoo, Phys. Rev. A **92**, 031402 (2015), URL <http://link.aps.org/doi/10.1103/PhysRevA.92.031402>.
- [59] B. K. Sahoo, R. G. E. Timmermans, B. P. Das, and D. Mukherjee, Phys. Rev. A **80**, 062506 (2009), URL <http://link.aps.org/doi/10.1103/PhysRevA.80.062506>.
- [60] M. S. Safronova, D. Jiang, B. Arora, C. W. Clark, M. G. Kozlov, U. I. Safronova, and W. R. Johnson, IEEE Trans. Ultrason. Ferroelectrics and Frequency Control **57**, 94 (2010).
- [61] P.-L. Liu, Y. Huang, W. Bian, H. Shao, H. Guan, Y.-B. Tang, C.-B. Li, J. Mitroy, and K.-L. Gao, Phys. Rev. Lett. **114**, 223001 (2015), URL <http://link.aps.org/doi/10.1103/PhysRevLett.114.223001>.
- [62] W. R. Johnson, S. A. Blundell, and J. Sapirstein, Phys. Rev. A **37**, 307 (1988).

1. Supplemental: Dirac-Fock basis sets

In Tables XII, XIII, and XIV we list the optimized S-spinor basis sets that were used to compute the energies shown in the main paper Table I.

2. Supplemental: polarizability breakdowns

We present in Table XV the breakdowns of the $5s_{\frac{1}{2}}$ and $5p_{\frac{3}{2}}$ (for $m_j = \frac{1}{2}$) at both $\omega = 0$ and at the magic wavelengths.

We present in Table XVI and breakdowns of the $5s_{\frac{1}{2}}$ and $5p_{\frac{3}{2}}$ (for $m_j = \frac{3}{2}$) at both $\omega = 0$ and at the magic wavelengths.

We present in Table XVII the breakdowns of the $5s_{\frac{1}{2}}$ and $4d_{\frac{5}{2}}$ at both $\omega = 0$ and at the magic wavelengths.

We present in Table XVIII the breakdowns of the $5s_{\frac{1}{2}}$ and $4d_{\frac{3}{2}}$ at both $\omega = 0$ and at the magic wavelengths.

TABLE XII: The exponents, λ_i , of S-spinor basis for the closed-shell state of the alkali-metal atoms

Li ⁺	Na ⁺		K ⁺		Rb ⁺			Cs ⁺		
<i>7s</i>	<i>7s</i>	<i>4p</i>	<i>8s</i>	<i>7p</i>	<i>11s</i>	<i>8p</i>	<i>5d</i>	<i>14s</i>	<i>12p</i>	<i>10d</i>
15.00000	17.478901	8.906343	22.790000	21.700000	54.542112	36.000000	20.676607	117.539065	50.898116	44.421251
8.00000	10.588106	4.706615	17.292481	11.552057	36.714627	28.566009	11.413245	83.361039	36.617350	31.729465
4.69873	7.376552	2.516997	10.488771	7.027067	30.744640	17.212806	7.057890	59.121304	26.343417	22.663903
2.47673	3.908322	1.581117	5.372695	5.273478	17.639600	12.762750	4.679490	41.930003	18.952099	16.188502
1.63200	2.644974		4.612349	3.189831	14.845074	5.836649	3.013206	29.737591	13.634603	11.563216
1.07000	2.016045		2.685122	2.301755	7.435420	4.475461		21.090490	9.809067	8.259440
0.66055	1.084267		1.797145	1.641334	6.200901	1.892352		14.957794	7.056883	5.899600
			0.969078		3.547780	1.413277		10.608365	5.076894	4.214000
					2.285862			7.523663	3.652442	3.010000
					1.729660			5.335931	2.627656	2.150000
					1.462792			3.784348	1.890400	
								2.683935	1.360000	
								1.903500		
								1.350000		

TABLE XIII: The exponents, λ_i , of S-spinor basis for the closed-shell state of the noble gas atoms

Ne	Ar		Kr			Xe			
<i>8s</i>	<i>5p</i>	<i>11s</i>	<i>9p</i>	<i>10s</i>	<i>9p</i>	<i>5d</i>	<i>14s</i>	<i>12p</i>	<i>9d</i>
45.399135	8.478657	34.980000	21.819460	55.509710	29.485877	18.970734	75.251507	35.791162	32.432647
26.975125	4.900173	27.650027	16.993680	35.893641	17.401415	10.615817	53.588918	25.360241	22.627481
16.028001	2.832016	19.938400	10.964770	30.521126	14.896787	6.554858	38.160646	17.969292	15.786651
9.523470	1.636742	16.931250	7.482350	16.222298	9.460614	4.324848	27.174179	12.732349	11.013968
5.658628	0.945942	12.295700	6.139970	15.137969	6.280458	2.647825	19.350721	9.021653	7.684182
3.362227		7.384180	3.380570	9.419056	4.517666		13.779640	6.392397	5.361070
1.997758		5.871280	2.775260	6.515549	3.649240		9.812476	4.529406	3.740290
1.187022		3.985270	1.471470	3.780907	2.269718		6.987460	3.209363	2.609511
		1.519523	0.994720	2.580124	1.453805		4.975767	2.274031	1.820593
		1.290069		1.826235			3.543242	1.611291	
		0.897910					2.523141	1.141699	
							1.796728	0.808964	
							1.279449		
							0.911095		

TABLE XIV: The exponents, λ_i , of S-spinor basis for the closed-shell state of the alkaline-earth atoms

Be ²⁺		Mg ²⁺		Ca ²⁺		Sr ²⁺		Ba ²⁺		
5s	9s	6p	10s	9p	12s	10p	5d	15s	14p	10d
20.645400	20.000000	20.291000	39.220281	59.809200	78.966521	35.880469	21.271807	116.958344	47.985577	45.454303
6.548210	12.980000	9.086105	27.331206	18.309400	56.404658	23.920312	11.766205	85.060614	35.544872	32.467359
3.521360	10.987200	5.384429	19.046137	11.621200	40.289041	15.946875	7.246050	61.862265	26.329535	23.190971
2.423980	6.826120	3.016046	13.272569	7.243230	28.777887	10.631250	4.827920	44.990738	19.503359	16.564979
0.733843	2.808800	1.485000	9.249177	5.090000	20.555633	7.087500	3.105406	32.720537	14.446933	11.832128
	1.982660	1.352222	6.445420	4.430000	14.682595	4.725000		23.796754	10.701432	8.451520
	1.209417		4.491582	2.677958	10.487568	3.150000		17.306730	7.926986	6.036800
	0.986366		3.130022	2.063877	7.491120	2.100000		12.586713	5.871842	4.312000
	0.751237		2.181200	1.489720	5.350800	1.400000		9.153973	4.349512	3.080000
			1.520000		3.822000	2.600000		6.657435	3.221861	2.200000
					2.730000			4.841771	2.386564	
					1.950000			3.521288	1.767825	
								2.560937	1.309500	
								1.862499	0.970000	
								1.354545		

TABLE XV: The contributions of individual transitions to the polarizabilities (in a.u.) of the $5s_{\frac{1}{2}}$ and $5p_{\frac{3}{2},m=\frac{1}{2}}$ states at the magic wavelengths. These results assume linearly-polarized light. $\delta\lambda$ are uncertainties calculated by assuming certain matrix elements have $\pm 2\%$ uncertainties.

ω (a.u.)	0	0.04536049	0.06425984	0.1038352	0.1086593
λ (nm)	∞	1004.4722	709.0487	438.8044	419.3232
$\delta\lambda$ (nm)		0.02	15	0.5	0.02
Ref. [58] (nm)		1004.47	716.72	438.37	419.30
		$5s_{\frac{1}{2}}$			
$5p_{\frac{1}{2}}$	28.6439	34.7716	44.3176	374.0870	-2551.0885
$5p_{\frac{3}{2}}$	55.4498	66.3984	82.8749	407.8492	1030.5370
$6p_{\frac{1}{2}}$	0.0027	0.0027	0.0028	0.0032	0.0033
$6p_{\frac{3}{2}}$	0.0001	0.0001	0.0001	0.0001	0.0001
Remainder	0.1864	0.1879	0.1894	0.1945	0.1953
Core	5.8128	5.8214	5.8300	5.8579	5.8623
Total	90.0957	107.1821	133.2148	788.0019	-1514.4906
		$5p_{\frac{3}{2}} (m = \frac{1}{2})$			
$5s_{\frac{1}{2}}$	-55.4498	-66.3984	-82.8749	-407.8492	-1030.5370
$4d_{\frac{3}{2}}$	-1.3958	-1317.0076	1.3892	0.3296	0.2950
$4d_{\frac{5}{2}}$	-78.9377	1369.5704	70.3193	17.3793	15.5727
$6s_{\frac{1}{2}}$	37.5051	45.9523	59.4297	1020.4421	-684.0269
$5d_{\frac{3}{2}}$	0.9704	1.1025	1.2774	2.6050	3.1017
$5d_{\frac{5}{2}}$	51.6420	58.6193	67.8494	137.2366	162.9085
Remainder	9.0997	9.5223	9.9947	11.9506	12.3331
Core	5.8128	5.8214	5.8300	5.8579	5.8623
Total	-30.7531	107.1821	133.2148	788.0019	-1514.4906

TABLE XVI: The contributions of individual transitions to the polarizabilities (in a.u.) of the $5s_{\frac{1}{2}}$ and $5p_{\frac{3}{2},m=\frac{3}{2}}$ states at the magic wavelengths. These results assume linearly-polarized light. $\delta\lambda$ are uncertainties calculated by assuming certain matrix elements have $\pm 2\%$ uncertainties.

ω (a.u.)	0	0.04512102	0.06316610	0.1093628
λ (nm)	∞	1009.8032	721.3260	416.6258
$\delta\lambda$ (nm)		0.2	10	0.02
Ref. [58] (nm)		1009.80	724.92	416.62
		$5s_{\frac{1}{2}}$		
$5p_{\frac{1}{2}}$	28.6439	34.6935	43.5140	-1175.6343
$5p_{\frac{3}{2}}$	55.4498	66.2606	81.5142	1335.6567
$6p_{\frac{1}{2}}$	0.0027	0.0027	0.0028	0.0033
$6p_{\frac{3}{2}}$	0.0001	0.0001	0.0001	0.0001
Remainder	0.1864	0.1878	0.1893	0.1954
Core	5.8128	5.8213	5.8294	5.8629
Total	90.0957	106.9660	131.0497	166.0840
		$5p_{\frac{3}{2}} (m = \frac{3}{2})$		
$5s_{\frac{1}{2}}$	0.0000	0.0000	0.0000	0.0000
$4d_{\frac{3}{2}}$	-12.5624	-1084.8929	13.4056	2.6136
$4d_{\frac{5}{2}}$	-52.6251	1131.7423	50.0752	10.2228
$6s_{\frac{1}{2}}$	0.0000	0.0000	0.0000	0.0000
$5d_{\frac{3}{2}}$	8.7340	9.9079	11.3754	28.7347
$5d_{\frac{5}{2}}$	34.4280	39.0240	44.7588	111.7330
Remainder	5.1321	5.3621	5.6053	6.9170
Core	5.8128	5.8213	5.8294	5.8629
Total	-11.0806	106.9660	131.0497	166.0840

TABLE XVII: The contributions of individual transitions to the polarizabilities (in a.u.) of the $5s_{\frac{1}{2}}$ and $4d_{\frac{5}{2}}$ states at the magic wavelengths. These results assume linearly-polarized light. $\delta\lambda$ are uncertainties calculated by assuming certain matrix elements have $\pm 2\%$ uncertainties.

ω (a.u.)	0	0.02423070	0.1092601	0.1092616	0.1092647
λ (nm)	∞	1880.3976	417.0175	417.0116	416.9999
$\delta\lambda$ (nm)		103	0.0014	0.0016	0.0010
Ref. [58](nm)	∞		417.01	417.00	417.00
$5s_{\frac{1}{2}}$					
$5p_{\frac{1}{2}}$	28.6439	30.1606	-1276.3995	-1274.7701	-1271.5180
$5p_{\frac{3}{2}}$	55.4498	58.1876	1280.1591	1280.9529	1282.5461
Remainder	0.1891	0.1895	0.1988	0.1988	0.1988
Core	5.8128	5.8153	5.8628	5.8628	5.8628
Total	90.0957	94.3530	9.8211	12.2444	17.0897
$4d_{\frac{5}{2}}$					
	Average	$m_j = \frac{3}{2}$	$m_j = \frac{1}{2}$	$m_j = \frac{3}{2}$	$m_j = \frac{5}{2}$
$5p_{\frac{3}{2}}$	43.8543	75.3721	-15.3687	-10.2455	0.0000
$6p_{\frac{3}{2}}$	0.0045	0.0055	0.0122	0.0081	0.0000
$4f_{\frac{5}{2}}$	0.3316	0.2592	0.0389	0.3503	0.9732
$4f_{\frac{7}{2}}$	6.6273	7.1963	11.6713	9.7262	5.8358
$7p_{\frac{3}{2}}$	0.0009	0.0010	0.0019	0.0013	0.0000
$5f_{\frac{5}{2}}$	0.0859	0.0669	0.0090	0.0810	0.2250
$5f_{\frac{7}{2}}$	1.7167	1.8560	2.6979	2.2483	1.3490
Remainder	3.5576	3.7808	4.8957	4.2118	2.8439
Core	5.8128	5.8153	5.8628	5.8628	5.8628
Total	61.9916	94.3530	9.8211	12.2444	17.0897

TABLE XVIII: The contributions of individual transitions to the polarizabilities (in a.u.) of the $5s_{\frac{1}{2}}$ and $4d_{\frac{3}{2}}$ states at the magic wavelengths. These results assume linearly-polarized light. $\delta\lambda$ are uncertainties calculated by assuming certain matrix elements have $\pm 2\%$ uncertainties.

ω (a.u.)	0	0.04204437	0.04532277	0.1092607	0.1092636
λ (nm)	∞	1083.6969	1005.3081	417.0149	417.0038
$\delta\lambda$ (nm)		4	0.011	0.0017	0.0012
Ref. [58] (nm)		1082.38	1005.30	417.00	417.00
$5s_{\frac{1}{2}}$					
$5p_{\frac{1}{2}}$	28.6439	33.7544	34.7592	-1275.7000	-1272.5909
$5p_{\frac{3}{2}}$	55.4498	64.6016	66.3766	1280.4995	1282.0191
Remainder	0.1891	0.1904	0.1907	0.1988	0.1988
core	5.8128	5.8202	5.8214	5.8628	5.8628
Total	90.0957	104.3666	107.1479	10.8611	15.4898
$4d_{\frac{3}{2}}$					
	Average	$m_j = \frac{3}{2}$	$m_j = \frac{1}{2}$	$m_j = \frac{1}{2}$	$m_j = \frac{3}{2}$
$5p_{\frac{1}{2}}$	38.2884	0.0000	-426.7411	-13.0801	0.0000
$5p_{\frac{3}{2}}$	6.9791	88.6061	513.0793	-0.2911	-2.6193
$6p_{\frac{1}{2}}$	0.0011	0.0000	0.0023	0.0032	0.0000
$6p_{\frac{3}{2}}$	0.0010	0.0018	0.0002	0.0003	0.0026
$4f_{\frac{5}{2}}$	6.7604	5.6307	8.5027	11.0630	7.3755
$7p_{\frac{1}{2}}$	0.0002	0.0000	0.0004	0.0005	0.0000
$7p_{\frac{3}{2}}$	0.0002	0.0003	0.0000	0.0000	0.0004
$5f_{\frac{5}{2}}$	1.7645	1.4503	2.1852	2.5826	1.7217
Remainder	3.5164	2.8571	4.2974	4.7197	3.1460
core	5.8128	5.8202	5.8214	5.8628	5.8628
Total	63.1242	104.3666	107.1479	10.8611	15.4898